Calibration of Strapdown Magnetometers in Magnetic Field Domain

Demoz Gebre-Egziabher[1]; Gabriel H. Elkaim[2]; J. David Powell[3]; and Bradford W. Parkinson[4]

Abstract: This paper presents an algorithm for calibrating strapdown magnetometers in the magnetic field domain. In contrast to the traditional method of compass swinging, which computes a series of heading correction parameters and thus is limited to use with two-axis systems, this algorithm estimates magnetometer output errors directly. Therefore, this new algorithm can be used to calibrate a full three-axis magnetometer triad. The calibration algorithm uses an iterated, batch least-squares estimator that is initialized using a two-step nonlinear estimator. The algorithm is simulated to validate convergence characteristics and further validated on experimental data collected using a magnetometer triad. It is shown that the postcalibration residuals are small and result in a system with heading errors on the order of 1 to 2 degrees.

DOI: 10.1061/(ASCE)0893-1321(2006)19:2(87)

CE Database subject headings: Calibration; Magnetic fields; Algorithms; Aerospace engineering.

Introduction

Magnetometers measure the intensity of magnetic fields and are used in many scientific and engineering applications. In vehicle navigation, for example, they are used as inexpensive heading sensors (where heading is the angle between the vehicle and north). In these applications, heading is determined by measuring the horizontal component of Earth's magnetic field vector, $\mathbf{h}$, using a perpendicular pair (or an orthogonal triad) of magnetometers. A magnetometer triad would measure $\mathbf{h}^b=[h_x^b h_y^b h_z^b]^T$, which, as indicated by the superscript b, is Earth's magnetic field vector $\mathbf{h}$ expressed in a coordinate frame fixed to the body of the vehicle. A pair of magnetometers would measure only two components of the field vector or $\mathbf{h}^b=[h_x^b h_y^b]^T$.

If the the $x-y$ plane of the body coordinate system is level (i.e., parallel to Earth's local tangent), the magnetometer readings are used to compute heading with respect to magnetic north using the following formula:

$$\psi = -\tan^{-1}\left(\frac{h_y^b}{h_x^b}\right) \tag{1}$$

The negative sign in Eq. (1) ensures that clockwise heading angles (measured from north) are positive when the magnetometer measurements are parametrized using the standard aerospace body axis convention (a body axis system where the $x-y$ plane is parallel to the local tangent and the positive z-axis is pointing down when the vehicle is level). If the $x-y$ plane is not physically level, it can be leveled analytically by measuring the pitch and roll angles of the vehicle. These angles are used to compute the body-to-locally level transformation matrix, $\overset{b\to w}{\mathbf{C}}$, which is used to map the magnetometer measurement to the locally level plane. Note that $\overset{b\to w}{\mathbf{C}}$ is the b to w coordinate frame transformation matrix where the w is the $x-y-z$ coordinate frame having its x-axis coincident with the vehicle's longitudinal axis and its $x-y$ plane level or parallel to the local tangent. This coordinate frame is sometimes called the wander azimuth plane (Siouris 1993).

Since the output of any sensor is to some degree corrupted by errors, the actual measurement made by the pair or triad of magnetometers, $\hat{\mathbf{h}}^b$, will be different from the true magnetic field $\mathbf{h}^b$. The process of estimating these errors and removing them from the magnetometer measurements is the subject of this paper.

For heading determination systems that use a pair of perpendicular magnetometers, a well-known calibration procedure called compass swinging has been used successfully (Bowditch 1984). The compass swinging procedure involves leveling and rotating the vehicle containing the magnetometers through a series of N known headings, as shown schematically in Fig. 1. The differences between the heading determined using the magnetometer outputs and the N known headings are used to compute calibration parameters. This procedure is discussed in more detail later in the paper.

Compass swinging has several shortcomings, however, which make it unsuitable for many current applications. Two of the most significant shortcomings of this procedure are that (1) it requires an external or independent source of heading; and (2) the plane containing the pair of magnetometers must be level. These two factors limit or even preclude in situ calibration because the magnetometer being calibrated is normally the only source of heading

[1]Assistant Professor, Dept. of Aerospace Engineering and Mechanics, Univ. of Minnesota, Twin Cities, 110 Union St., N.E., 107 Akerman Hall, Minneapolis, MN 55455. E-mail: gebre@aem.umn.edu

[2]Assistant Professor, Computer Engineering Dept., Univ. of California, Santa Cruz, 1156 High St., Santa Cruz, CA 95064. E-mail: elkaim@soe.ucsc.edu

[3]Professor Emeritus, Dept. of Aeronautics and Astronautics, Stanford Univ., Durand Building, 496 Lomita Mall, Stanford, CA 94305-4035. E-mail: jdpowell@stanford.edu

[4]Professor Emeritus, Dept. of Aeronautics and Astronautics, Stanford Univ., Durand Building, 496 Lomita Mall, Stanford, CA 94305-4035. E-mail: brad@relgyro.stanford.edu

Note. Discussion open until September 1, 2006. Separate discussions must be submitted for individual papers. To extend the closing date by one month, a written request must be filed with the ASCE Managing Editor. The manuscript for this paper was submitted for review and possible publication on February 2, 2004; approved on March 22, 2005. This paper is part of the *Journal of Aerospace Engineering*, Vol. 19, No. 2, April 1, 2006. ©ASCE, ISSN 0893-1321/2006/2-87–102/$25.00.

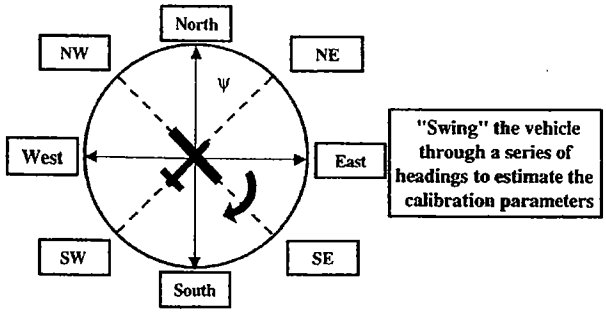

Fig. 1. Graphical description of swinging

information. Furthermore, the b and w coordinate frames will not always be coincident.

Another deficiency of compass swinging is that it is a heading domain calibration algorithm. That is, it involves computing a series of heading correction parameters that, when added to heading [as computed by Eq. (1)], cancel heading deviations caused by magnetometer errors. Thus, the algorithm is not applicable for applications other than heading determination, such as three-axis attitude determination as discussed in Gebre-Egziabher et al. (2001a,b), Gebre-Egziabher (2001), and Elkaim (2001). Another shortcoming of compass swinging is that the quality of the calibration degrades as the vehicle with the magnetometers is moved farther away from the geographical point where the calibration was performed. This is because the correction parameters computed are functions of the local magnetic field strength.

Recently, different magnetometer calibration methodologies that deal with some of the shortcomings of compass swinging have been proposed. For example, Caruso (2000) proposed a method that computes correction parameters for the magnetometer's field measurement errors instead of heading correction parameters. Since this is a procedure for calibration in the magnetic field domain, unlike compass swinging, the results are location independent. In addition, the calibration is not limited to magnetometers used solely for heading determination but is applicable in cases where the magnetometers are used for any purpose (Gebre-Egziabher et al. 2001a,b). However, the method discussed in Caruso (2000) does have some limitations. For example, it still requires that the $x-y$ body plane of the vehicle containing the magnetometers be level during calibration, which severely limits the algorithm from real-time use in a vehicle that is moving.

To improve the performance of the above-discussed magnetic field domain calibration procedure, this paper presents a reformulation and extension of the method discussed in Caruso (2000). First, a unified error model for strapdown magnetometers is presented, and then the problem of calibrating strapdown magnetometers in the context of the unified error model is discussed. Prior art in calibration of magnetometers is then presented. In particular, we will discuss compass swinging or the classical method of calibrating magnetometers in the heading domain. This will serve as a motivation for the methods presented in this paper as well as a benchmark against which we will compare these new calibration methods. The algorithm development section of the paper will introduce an iterative, batch least-squares algorithm for calibration in the magnetic field domain. We will also present a two-step, nonlinear estimator used to establish the initial conditions for the iterative, batch least-squares algorithm, followed by the results of simulation and trade studies as well as experimental results that validate the algorithms developed. Concluding remarks and a discussion of future algorithm improvements close the paper.

Error Modeling

The outputs of magnetometers are corrupted by wide-band measurement noise, stochastic biases due to sensor imperfections, installation errors, and unwanted magnetic interference in the vicinity of the sensors.

The unwanted or interfering magnetic fields can be classified into two distinct groups. The first group consists of constant or slowly time-varying fields generated by primarily ferromagnetic structural materials in the proximity of the magnetometers. The field measurement errors resulting from such interferences are referred to as hard iron biases (Kayton and Fried 1997).

The second group of interfering magnetic fields result from materials that generate their own magnetic field in response to an externally applied field. This generated field is affected by both the magnitude and direction of the externally applied magnetic field. Such materials are called soft irons, and the error they generate is referred to as a soft iron bias. In a moving vehicle, the orientation of Earth's magnetic field relative to the vehicle (and any soft iron materials contained therein) changes continuously. Thus, the resulting soft iron errors are time varying.

A comprehensive mathematical model for the output error of a strapdown magnetometer can be written as

$$\hat{\mathbf{h}}^w = \overset{b\to w}{\mathbf{C}}\,[C_m C_{sf} C_{si}(h^b + b^b + w^b)] \tag{2}$$

In this model, $\hat{\mathbf{h}}^w$=measured (or estimated) field measurement in the w plane while $\mathbf{b}^b=[b_x^b b_y^b b_z^b]^T$ and $\mathbf{w}^b=[w_x^b w_y^b w_z^b]^T$ represent hard iron biases and wide-band noise, respectively, and are additive errors that corrupt the true field measurement $\mathbf{h}^b$. The variables $\mathbf{C}_{si}$, $\mathbf{C}_{sf}$, and $\mathbf{C}_m$ are 3×3 matrices that account for soft iron, scale factor, and misalignment errors, respectively. The matrix $\overset{b\to w}{\mathbf{C}}$ is the 3×3 body-to-local-tangent transformation matrix discussed earlier. These errors are discussed next in more detail.

Hard Iron Errors (b^b)

Normally, the largest errors tend to be null shifts caused by unwanted magnetic fields in the vicinity of the magnetometers. This can be seen clearly by examining Fig. 2, which shows the output error from a magnetometer measuring the vertical component of Earth's magnetic field vector, $\mathbf{h}_z^b$, at Stanford, California (approximately $N37.5°$ latitude and $W122.1°$ longitude). Earth's magnetic field vector at this location, $\mathbf{h}$, in north-east-down (NED) coordinates is equal to $[0.23199\ 0.06361\ 0.43500]^T$ Gauss (Barton 1997). Fig. 2 shows the output of a magnetometer measuring the vertical component after h_z (0.43500 Gauss) has been subtracted. What is shown in the figure, therefore, is a null shift of 92 milli-Gauss and the largest component of the output error.

Wideband Noise (σ_w)

Removing the null shift from the data shown in Fig. 2 leaves errors due to magnetometer measurement wideband noise. Fig. 3 is a histogram of the data shown in Fig. 2. From Fig. 3, observe that the wideband noise has a standard deviation, σ_w, of approximately 5 milli-Gauss, which is smaller than the null shift.

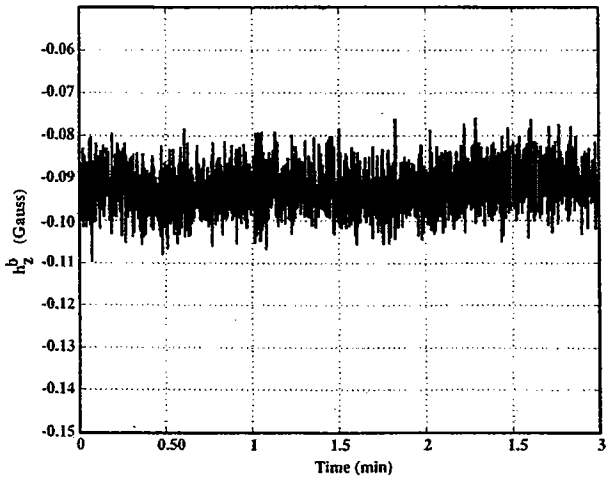

Fig. 2. Magnetometer null-shift time history (output from Honeywell HMC2003 magnetometer triad)

Soft Iron Errors (C_{si})

Even though it is not always valid, in this work we assume that a linear relationship (without hysteresis) exists between the field a soft iron generates and the externally applied field to which it responds. For the application that motivated this work—heading determination in aircraft—the assumption of no hysteresis is reasonable for two reasons. First, aircraft structures are normally made from nonferromagnetic materials that do not exhibit the aforementioned hysteresis (e.g., aluminum or composites). Second, even if ferromagnetic materials are present in the vicinity of the magnetometers, the externally applied field would have to be very large relative to Earth's magnetic field before the hysteresis loop becomes an issue. If care is taken during installation such that objects that generate large magnetic fields (e.g., large permanent magnets or current carrying wires) are not located in the vicinity of the magnetometers, then hysteresis will not be an issue even if ferromagnetic materials are located close to the sensors. Thus, assuming no hysteresis, $\mathbf{C}_{si}$ can be written as

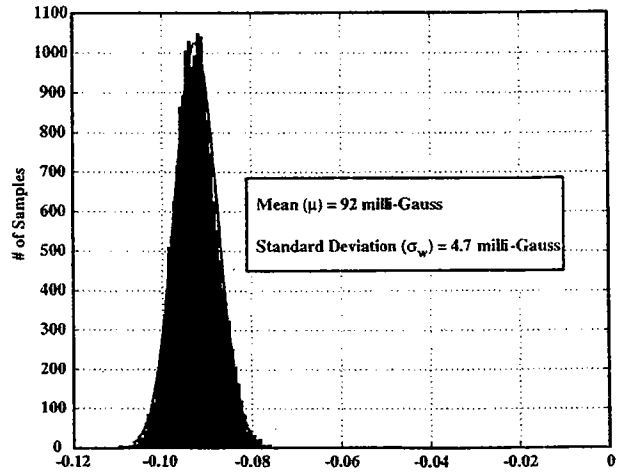

Fig. 3. Histogram of magnetometer output error shown in Fig. (2)

$$\mathbf{C}_{si} = \begin{bmatrix} \alpha_{xx} & \alpha_{xy} & \alpha_{xz} \\ \alpha_{yx} & \alpha_{yy} & \alpha_{yz} \\ \alpha_{zx} & \alpha_{zy} & \alpha_{zz} \end{bmatrix} \tag{3}$$

The α_{ij} terms represent the effective soft iron coefficients and are the constants of proportionality between the magnetic field applied to a soft iron and the resulting induced magnetic field. From a notation point of view, α_{xy}, for example, represents the effective coefficient relating the field generated in the x-direction in response to an applied field in the y-direction. The term effective is used to describe these coefficients because they represent the effect of all soft iron material present that may corrupt the magnetometer outputs (Gebre-Egziabher 2001; Elkaim 2001).

Scale Factor (C_{sf})

Scale-factor errors are modeled using the 3×3 matrix $\mathbf{C}_{sf}$ given by

$$\mathbf{C}_{sf} = \begin{bmatrix} (1+s_{fx}) & 0 & 0 \\ 0 & (1+s_{fy}) & 0 \\ 0 & 0 & (1+s_{fz}) \end{bmatrix} \tag{4}$$

The scale factor errors s_{fx}, s_{fy}, and s_{fz} represent the uncertainty in knowledge of the constant of proportionality relating magnetometer input to output.

Misalignments (C_m)

In an ideal installation, the magnetometer triad will be mounted in perfect alignment with the body axis of the aircraft. Stated differently, the magnetometer axes will be identical to the body axes. In actual practice, perfect alignment cannot always be achieved. The matrix $\mathbf{C}_m$ accounts for this misalignment and represents the residual error in our knowledge of the magnetometer axes (sensor platform or p axes) to body frame transformation matrix $\overset{p\to b}{\mathbf{C}}$. Since by definition residual misalignment errors are very small (but not negligible), $\mathbf{C}_m$ can be modeled as the following skew-symmetric matrix:

$$\mathbf{C}_m = \begin{bmatrix} 1 & -\epsilon_z & \epsilon_y \\ \epsilon_z & 1 & -\epsilon_x \\ -\epsilon_y & \epsilon_x & 1 \end{bmatrix} \tag{5}$$

The three independent parameters defining the matrix (ϵ_x, ϵ_y, and ϵ_z) represent small rotations about the body axes of the vehicle that will bring the platform axes into perfect alignment with the body axes. Thus, $\mathbf{C}_m$ is constant and only needs to be estimated once. Note that the error model given by Eq. (2) and the definition of $\mathbf{C}_m$ given by Eq. (5) do not imply that in an error-free installation the magnetometer and body axes of the vehicle are aligned. The magnetometer triad can be installed in any known orientation relative to the body frame. In this instance, the transformation matrix $\overset{b\to w}{\mathbf{C}}$ from Eq. (2) can be redefined as the magnetometer triad-to-local-tangent transformation matrix. The matrix $\mathbf{C}_m$ will represent the error in our knowledge of the magnetometer triad-to-body transformation matrix.

The process of calibrating a pair or triad of magnetometers involves estimating the various unknown vectors and matrices defined in Eqs. (2)–(5). Methods for estimating these unknown parameters are the subject of the remainder of this paper.

Compass Swinging

The compass swinging algorithm has been used for some time in marine (Bowditch 1995) and aviation (LITEF 2001) applications. In these applications, the sensors traditionally used were a pair of flux-gate or flux-valve magnetometers. The sensors are arranged perpendicular to each other and coincident with the x and y body axes of the vehicle. For these systems, the heading error, $\delta\psi$, due to both hard and soft iron biases is given by

$$\delta\psi = A + B\sin(\psi) + C\cos(\psi) + D\sin(2\psi) + E\cos(2\psi) \quad (6)$$

This equation is derived in the appendix at the end of this paper, and from that derivation it can be seen that the coefficients A through E are functions of the soft iron coupling terms, α_{ij}, and Earth's local horizontal magnetic field strength, $\mathbf{h}_h$.

The unknown coefficients A through E are estimated by leveling and rotating the vehicle through a series of N known headings, as shown schematically in Fig. 1. At each known kth heading, the heading error, $\delta\psi_k$, is computed and used to form the following system of equations:

$$\begin{bmatrix} \delta\psi_1 \\ \delta\psi_2 \\ \vdots \\ \delta\psi_N \end{bmatrix} = \begin{bmatrix} 1 & \sin(\psi_1) & \cos(\psi_1) & \sin(2\psi_1) & \cos(2\psi_1) \\ 1 & \sin(\psi_2) & \cos(\psi_2) & \sin(2\psi_2) & \cos(2\psi_2) \\ \vdots & & \ddots & & \vdots \\ 1 & \sin(\psi_N) & \cos(\psi_N) & \sin(2\psi_N) & \cos(2\psi_N) \end{bmatrix} \begin{bmatrix} A \\ B \\ C \\ D \\ E \end{bmatrix} \quad (7)$$

A batch least-squares solution of Eq. (7) yields estimates for the coefficients A through E.

Examination of Eqs. (6) and (7) reveals at least two short comings of the compass swinging procedure. First, the fact that the coefficients A through E are functions of $\mathbf{h}_h$ (see Appendix) implies that the calibration is location dependent. Thus, if the vehicle is expected to travel over large distances, multiple calibrations must be performed due to variations in Earth's magnetic field.

The second shortcoming of compass swinging becomes apparent when we note that heading is a required input to the algorithm. Since heading errors due to hard and soft iron errors are heading dependent, the heading input into the algorithm will be corrupted by a nonconstant bias. Thus an independent measurement of heading is required when calibrating magnetometers using this method. In aviation applications, the standard practice is to use a compass rose painted on the tarmac similar to what is shown in Fig. 1 as the secondary independent heading measurement.

Calibration Algorithm

In addition to the above noted limitations, the fact that the vehicle containing the magnetometers has to be level during calibration prevents use of compass swinging in motion. To deal with this shortcoming, an alternative calibration algorithm has been developed that works with both a pair and a triad of magnetometers. We first develop the algorithm assuming that only a pair of magnetometers are used. Once the basic algorithm has been developed, it is extended to three dimensions such that it is applicable to magnetometer triads. The method developed corrects the field measurement errors directly, and not the effect of field measurement errors on heading. Thus, as noted earlier, we will refer to this as a method of calibration in the magnetic field domain.

The fundamental idea behind calibration in the magnetic field domain is that the locus of error-free measurements from a pair of perpendicular magnetometers is a circle. It is easy to show that this is the case by examining the expressions for h_x^b and h_y^b. From Fig. 1 it is clear that $h_x^b = h_h\cos(\psi)$ and $h_y^b = -h_h\sin(\psi)$. Squaring these expressions and adding them together leads to the following equation:

$$(h_x^b)^2 + (h_y^b)^2 = h_h^2\cos^2\psi + h_h^2\sin^2\psi = h_h^2 \quad (8)$$

This is the equation of a circle with its center at the origin. The radius of the circle is equal to the magnitude of the horizontal component of the local Earth magnetic field vector and is a function of geographical location. The magnitude of the radius varies with latitude, longitude, and altitude because Earth's magnetic field vector varies with location. This variation of Earth's magnetic field vector can be modeled with reasonable accuracy using the current International Geomagnetic Reference Field (IGRF) model (Barton 1997).

The effect of the various magnetometer errors described in Eq. (2) is to alter the shape of the locus of measurements described by Eq. (8). In this instance, as noted in Eq. (2), the erroneous x and y magnetometer outputs will be $\hat{h}_x^b$ and $\hat{h}_y^b$. Hard iron errors, for example, shift the origin of the basic locus, which can be shown mathematically by considering a hard iron bias vector with components b_x and b_y. If the x and y field measurements in the platform axes are biased by b_x and b_y, respectively, the equation for the locus of the magnetometer measurements becomes

$$(\hat{h}_x^b - b_x)^2 + (\hat{h}_y^b - b_y)^2 = h_h^2 \quad (9)$$

This is still the equation of a circle, but instead of having its center located at the origin, its center is at (b_x, b_y).

In the absence of other forms of errors, scale-factor errors cause the body x- and y-magnetometer measurements to be different when both are subjected to an identical magnetic field. This can be expressed mathematically as follows:

$$\hat{h}_x^b = (1 + s_{fx})h_h\cos\psi, \quad (10)$$

$$\hat{h}_y^b = -(1 + s_{fy})h_h\sin\psi. \quad (11)$$

Squaring Eqs. (10) and (11) and adding them together leads to

$$\left(\frac{\hat{h}_x^b}{1 + s_{fx}}\right)^2 + \left(\frac{\hat{h}_y^b}{1 + s_{fy}}\right)^2 = h_h^2 \quad (12)$$

which is the equation of an ellipse centered at the origin. The major and minor axes' magnitudes are determined by the scale-factor errors, s_{fx} and s_{fy}. When the hard iron errors b_x and b_y are included in Eqs. (10) and (11), the resulting locus is still an ellipse but its center is moved away from the origin to (b_x, b_y). That is

$$\left(\frac{\hat{h}_x^b - b_x}{1 + s_{fx}}\right)^2 + \left(\frac{\hat{h}_y^b - b_y}{1 + s_{fy}}\right)^2 = h_h^2 \quad (13)$$

Soft iron errors will modify the error-free circular locus into an ellipse but also rotate the major and minor axes of the ellipse. To show this mathematically, consider expressions for $\hat{\mathbf{h}}_x^b$ and $\hat{\mathbf{h}}_y^b$ when soft iron biases are the only sources of error. In this instance $\hat{h}_x^b$ and $\hat{h}_y^b$ become [see Eqs. (56) and (57) in the Appendix]

$$\hat{h}_x^b = h_h\cos\psi(1 + \alpha_{xx}) - \alpha_{xy}h_h\sin\psi \quad (14)$$

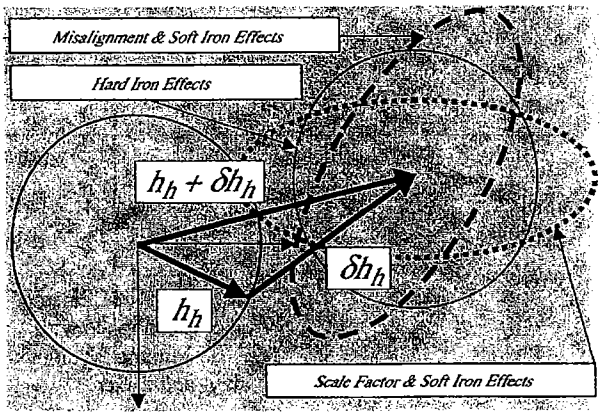

Fig. 4. Effect of errors on magnetic field measurement locus in 2D

$$\hat{h}_y^b = -h_h \sin\psi(1+\alpha_{yy}) - \alpha_{yx} h_h \cos\psi \tag{15}$$

In matrix form these equations become

$$\begin{bmatrix} \hat{h}_x^b \\ \hat{h}_y^b \end{bmatrix} = \begin{bmatrix} (1+\alpha_{xx}) & \alpha_{xy} \\ \alpha_{yx} & (1+\alpha_{yy}) \end{bmatrix} \begin{bmatrix} h_h \cos\psi \\ -h_h \sin\psi \end{bmatrix} \tag{16}$$

Inverting this matrix equation and noting that $h_x^b = h_h \cos(\psi)$ and $h_y^b = -h_h \sin(\psi)$ lead to the following:

$$\begin{bmatrix} h_x^b \\ h_y^b \end{bmatrix} = \frac{1}{(1+\alpha_{xx})(1+\alpha_{yy}) - \alpha_{xy}\alpha_{yx}} \begin{bmatrix} (1+\alpha_{yy}) & -\alpha_{xy} \\ -\alpha_{yx} & (1+\alpha_{xx}) \end{bmatrix} \begin{bmatrix} \hat{h}_x^b \\ \hat{h}_y^b \end{bmatrix} \tag{17}$$

If the two equations represented by this matrix are squared and added, the resulting locus will describe an ellipse with rotated major and minor axes. If hard iron errors are present in addition to soft iron errors, the locus will still be a rotated ellipse but its center will be displaced from the origin. Fig. 4 is a graphical summary of the effect of the various errors on the locus of magnetometer measurements.

For the remainder of this paper, we will assume that $\mathbf{C}_m$=identity matrix and α_{ij} is where $i \neq j$ is zero. The assumption that $\alpha_{ij}=0$ for $i \neq j$ is not always valid. In the application that motivated this work [general aviation or uninhabited aerial vehicle (UAV) heading determination], the assumption is reasonable because aircraft structures are normally made from aluminum or composite materials. This assumption is further validated by experimental data that will be discussed later in the paper. The data show that for a magnetometer installation in a wooden (composite) structure, the ellipse (or ellipsoid in the 3D case) had major and minor axes aligned with the body axes justifying the assumption that $\alpha_{ij}=0$ when $i \neq j$. Similarly, $\mathbf{C}_m$ was made to be the identity matrix by careful installation of the magnetometers and accounting for the residuals in postprocess.

Given the above assumptions (or simplifications), the hard iron errors affect the center of the elliptical measurement locus while the scale-factor errors and the α_{ii} soft iron terms affect the size of the major and minor axes. Thus the calibration algorithm that will be developed is nothing more than a parameter estimation problem. The algorithm is an attempt to fit the best ellipse (in the least-squares sense) to the measured magnetometer data.

In the case of a magnetometer triad, the error-free locus of outputs is a sphere. That will be centered at the origin with a radius equal to the magnitude of Earth's magnetic field vector. The various magnetometer errors alter the spherical locus into an ellipse and displace it from the center. In particular, the scale factor and α_{ii} soft iron terms reshape the sphere into an ellipsoid centered at the origin. Hard iron errors shift the ellipsoid away from the origin, and the effect of the wideband noise is to roughen the smooth surface of the measurement locus. Note that if $\alpha_{ij} \neq 0$, it implies that the major/minor axes of the ellipsoid are not aligned with the body axis, which means that additional states are required to completely describe the locus of measurements. Thus the algorithm that will be presented is not valid if α_{ij} for $i \neq j$ are significantly different from zero.

Thus the calibration algorithm is the problem of determining the parameters of an ellipsoid that best fits the data collected from a magnetometer triad. Mathematically, the locus of measurements is described by the following equation:

$$\|h\|^2 = h^2 = \left(\frac{\hat{h}_x^b - b_x}{\gamma_x}\right)^2 + \left(\frac{\hat{h}_y^b - b_y}{\gamma_y}\right)^2 + \left(\frac{\hat{h}_z^b - b_z}{\gamma_z}\right)^2 \tag{18}$$

where

$$\gamma_x = (1+s_{fx})(1+\alpha_{xx}) \tag{19}$$

$$\gamma_y = (1+s_{fy})(1+\alpha_{yy}) \tag{20}$$

$$\gamma_z = (1+s_{fz})(1+\alpha_{zz}) \tag{21}$$

The parameters to be estimated are the hard iron biases denoted by b_x, b_y, and b_z and the combined effect of scale-factor error and the α_{ii} soft iron terms denoted by γ_x, γ_y, and γ_z. The given or known inputs to the calibration algorithm are the measured magnetometer outputs, $\hat{h}_x^b$, $\hat{h}_y^b$, and $\hat{h}_z^b$, and the magnitude of Earth's magnetic field vector, $\|\hat{h}\|=\mathbf{h}$, in the geographic area where the calibration is being performed.

Least-Squares Estimation

We can fit an ellipsoid of revolution to the measured magnetic field data by using a batch least-squares estimator. Different approaches can be used to derive the estimator equations for fitting data to an ellipsoid. For example, one approach is discussed in Eberly (2001). The approach taken here is to linearize Eq. (18), which results in a set of equations that are easy to implement in a Kalman filter. The estimator will have as states perturbations of the ellipsoid parameters defined in Eqs. (18)–(21). Thus, given an initial guess of the unknown parameters, the estimated perturbations are sequentially added to the initial guess and the procedure is repeated until convergence is achieved.

To linearize Eq. (18), we note that the perturbation of $\|h\|$, written as δh, is given by Kaplan (1952)

$$-\delta h = \left(\frac{\hat{h}_x^b - b_x}{h\gamma_x^2}\right)\delta b_x + \left(\frac{\hat{h}_x^b - b_x}{\sqrt{h\gamma_x^3}}\right)^2 \delta\gamma_x + \left(\frac{\hat{h}_y^b - b_y}{h\gamma_y^2}\right)\delta b_y + \left(\frac{\hat{h}_y^b - b_y}{\sqrt{h\gamma_y^3}}\right)^2 \delta\gamma_y + \left(\frac{\hat{h}_z^b - b_z}{h\gamma_z^2}\right)\delta b_z + \left(\frac{\hat{h}_z^b - b_z}{\sqrt{h\gamma_z^3}}\right)^2 \delta\gamma_z \tag{22}$$

$$\zeta_x \delta b_x + \eta_x \delta\gamma_x + \zeta_y \delta b_y + \eta_y \delta\gamma_y + \zeta_z \delta b_z + \eta_z \delta\gamma_z \tag{23}$$

where $h=\|h\|$. Note that the measured magnetometer outputs $\hat{h}_x^b$, $\hat{h}_y^b$, and $\hat{h}_z^b$ are functions of time, even though, for the sake of clarity, we have dropped the explicit notation of time in Eq. (23).

That is, it should be noted that $\hat{h}_y^b$ is actually $\hat{h}_y^b(t=t_k)$ and corresponds to the x magnetometer field measurement at time step k. The same is true for the y and z field measurements. Thus, given field measurements from k time steps, Eq. (23) can be written as

$$\begin{bmatrix} \delta h_1 \\ \delta h_2 \\ \vdots \\ \delta h_N \end{bmatrix} = \begin{bmatrix} \zeta_{x_1} & \eta_{x_1} & \zeta_{y_1} & \eta_{y_1} & \zeta_{z_1} & \eta_{z_1} \\ \zeta_{x_2} & \eta_{x_2} & \zeta_{y_2} & \eta_{y_2} & \zeta_{z_2} & \eta_{z_2} \\ \zeta_{x_3} & \eta_{x_3} & \zeta_{y_3} & \eta_{y_3} & \zeta_{z_3} & \eta_{z_3} \\ \vdots & & \ddots & & & \vdots \\ \zeta_{x_{k-1}} & \eta_{x_{k-1}} & \zeta_{y_{k-1}} & \eta_{y_{k-1}} & \zeta_{z_{k-1}} & \eta_{z_{k-1}} \\ \zeta_{x_k} & \eta_{k_N} & \zeta_{k_N} & \eta_{k_N} & \zeta_{k_N} & \eta_{k_N} \end{bmatrix} \begin{bmatrix} \delta b_x \\ \delta \gamma_x \\ \delta b_y \\ \delta \gamma_y \\ \delta b_z \\ \delta \gamma_z \end{bmatrix} \tag{24}$$

Eq. (24) is in the form $\delta\mathbf{h}=H\ \delta\mathbf{x}$ where $\delta\mathbf{x}$ is the vector of unknowns given by

$$\delta\mathbf{x} = [\delta b_x\ \delta\gamma_x\ \delta b_y\ \delta\gamma_y\ \delta b_z\ \delta\gamma_z]^T \tag{25}$$

The vector $\delta\mathbf{h}$ is the difference between the known magnetic field vector magnitude and its magnitude as computed from the magnetometer outputs. That is, $\delta h_k = h_k - \hat{h}_k$ where h_k is computed from the IGRF model (Barton 1996) and $\hat{h}_k$ is computed as

$$\hat{h}_k = \sqrt{\hat{h}_x^b + \hat{h}_y^b + \hat{h}_y^b} \tag{26}$$

An estimate of the calibration parameters $\hat{b}_x$, b_y, $\hat{b}_z$, $\hat{\gamma}_x$, $\hat{\gamma}_y$, and $\hat{\gamma}_z$ is obtained by using the following iterative algorithm:

1. Select an initial guess for $\hat{b}_x$, b_y, $\hat{b}_z$, $\hat{\gamma}_x$, $\hat{\gamma}_y$, and $\hat{\gamma}_z$. The initial guess for γ_x, γ_y, and γ_z must be nonzero.
2. Using the values of $\hat{b}_x$, b_y, $\hat{b}_z$, $\hat{\gamma}_x$, $\hat{\gamma}_y$, and $\hat{\gamma}_z$, form Eq. (24).
3. Obtain a least-squares estimate for $\delta\mathbf{x}$, denoted by $\delta\hat{\mathbf{x}}$, as follows:

$$\delta\hat{\mathbf{x}} = (H^T H)^{-1} H^T \delta\mathbf{h} \tag{27}$$

4. Use the estimate for $\delta\hat{\mathbf{x}}$ and update the unknown parameters as follows [(+) denotes parameter after update and (−) denotes parameter before update]:

$$b_x(+) = b_x(-) + \delta\hat{\mathbf{x}}(1) \tag{28}$$

$$\gamma_x(+) = \gamma_x(-) + \delta\hat{\mathbf{x}}(2) \tag{29}$$

$$b_y(+) = b_y(-) + \delta\hat{\mathbf{x}}(3) \tag{30}$$

$$\gamma_y(+) = \gamma_y(-) + \delta\hat{\mathbf{x}}(4) \tag{31}$$

$$b_z(+) = b_z(-) + \delta\hat{\mathbf{x}}(5) \tag{32}$$

$$\gamma_z(+) = \gamma_z(-) + \delta\hat{\mathbf{x}}(6) \tag{33}$$

5. Compute the covariance matrix $\mathbf{P}$ (which is a measure of the quality of the calibration) by using

$$\mathbf{P} = \sigma_w^2 (H^T H)^{-1} \tag{34}$$

where σ_w=standard deviation of the magnetometer wideband noise.

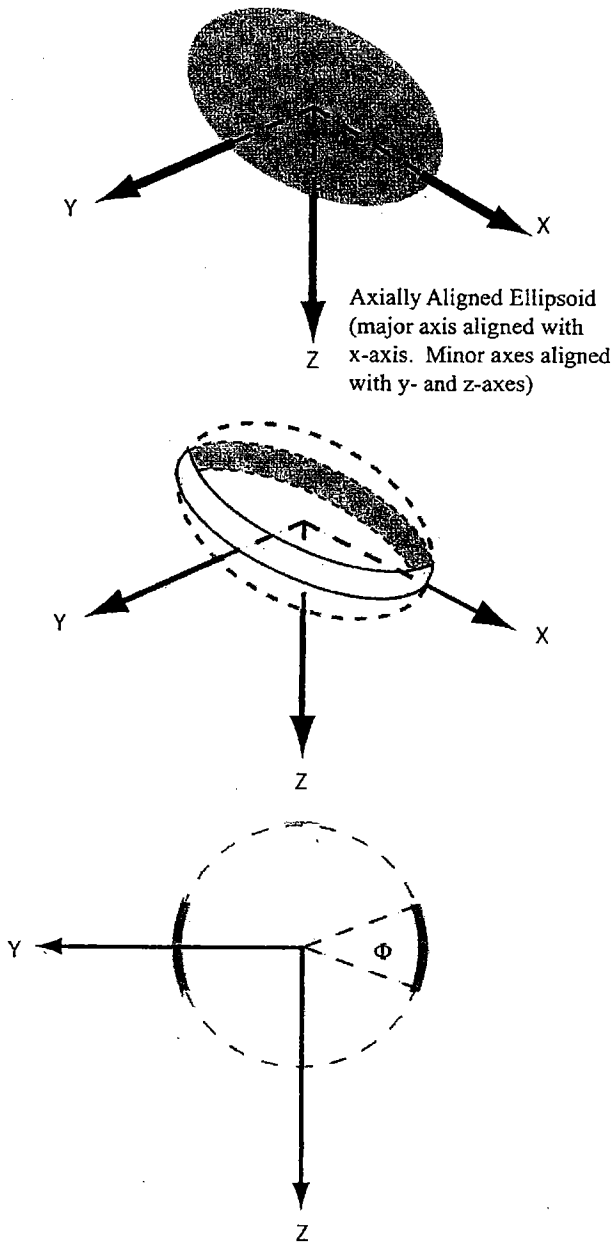

Fig. 5. Quantifying size of magnetometer measurement locus available for estimation

6. Return to Step (2) and repeat until convergence is achieved, which is when the estimate of b_x, b_y, b_z, γ_x, γ_y, and γ_z do not change from one iteration to the next.

The estimated calibration parameters can now be used to compute the corrected field measurements h_x^b, h_y^b, and h_z^b from the measured magnetometer readings $\hat{h}_x^b$, $\hat{h}_y^b$, and $\hat{h}_z^b$ using the following relations:

$$h_x^b = \frac{\hat{h}_x^b - \hat{b}_x}{\hat{\gamma}_x} \tag{35}$$

$$h_y^b = \frac{\hat{h}_y^b - \hat{b}_y}{\hat{\gamma}_y} \tag{36}$$

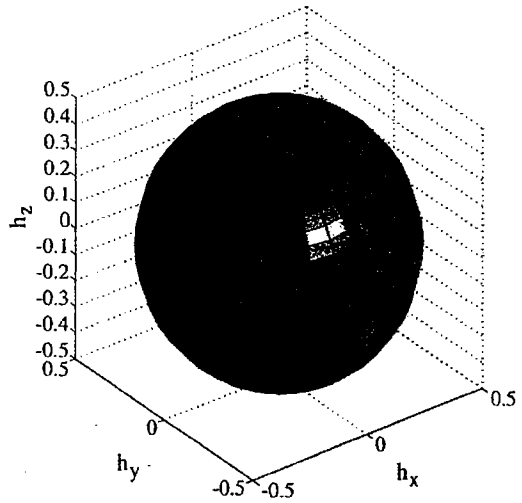

Fig. 6. Portion of ellipsoid representing locus of magnetometer measurements from actual experimental data. Data are shown by dark-color dots on smaller (inner) sphere. After calibration, locus of measurements will lie on larger outer sphere, which has radius equal to magnitude of local magnetic field vector.

$$h_z^b = \frac{\hat{h}_z^b - \hat{b}_z}{\hat{\gamma}_z} \tag{37}$$

As will be discussed in more detail later in the paper, the stability of the least-squares solution is sensitive to the following three factors:

1. Closeness of initial guess of hard iron biases and γ factors to their actual value;
2. Magnitude of wideband noise on magnetometer outputs; and
3. Shape and size of magnetometer measurement locus.

For a given set of magnetometer measurement data, the wideband noise on the sensor output and the size or shape of the measurement locus cannot be altered. Thus, to reduce the effect of these factors, a judicious selection of the magnetometers and data collection scheme must be performed; that is, nonalgorithmic mitigation techniques must be used. The effect of the initial conditions, however, can be mitigated algorithmically. In what follows, we will develop one such technique, which will be used to establish initial conditions.

Establishing Initial Conditions

The algorithms for establishing initial conditions use a nonlinear, two-step estimator that is an adaptation of an estimator presented in (Haupt 1996) and breaks the parameter identification problem given by Eq. (18) into two steps. In the first step, a first-step state vector is formed, the elements of which are algebraic combinations of the elements of the second-step state vector. The elements of the second-step state vector, on the other hand, are hard iron biases and those of the scale factor are soft iron γ terms. The estimation problem is linear in the first-step state and therefore retains the desirable properties of a linear system. Following estimation of the first-step states, elements of the second-step state vector are extracted through algebraic manipulation.

Derivation of the equations for the nonlinear two-step estimator begin by expanding Eq. (18) as follows:

Table 1. Parameters for Magnetometer Calibration Simulations

Case and strip size	Hard iron bias		Scale factor and soft iron		Wide band noise
I, 10°	b_x	1 Gauss	γ_x	4	5 milli-Gauss
	b_y	2 Gauss	γ_y	3	
	b_z	−3 Gauss	γ_z	2	
II, 20°	b_x	1 Gauss	γ_x	4	5 milli-Gauss
	b_y	2 Gauss	γ_y	3	
	b_z	−3 Gauss	γ_z	2	
III, 10°	b_x	1 Gauss	γ_x	4	10 milli-Gauss
	b_y	2 Gauss	γ_y	3	
	b_z	−3 Gauss	γ_z	2	
IV, 20°	b_x	1 Gauss	γ_x	4	10 milli-Gauss
	b_y	2 Gauss	γ_y	3	
	b_z	−3 Gauss	γ_z	2	

$$h^2 = \frac{(\hat{h}_x^b)^2 - 2(\hat{h}_x^b)(b_x) + (b_x)^2}{\gamma_x^2} + \frac{(\hat{h}_y^b)^2 - 2(\hat{h}_y^b)(b_y) + (b_y)^2}{\gamma_y^2} + \frac{(\hat{h}_z^b)^2 - 2(\hat{h}_z^b)(b_z) + (b_z)^2}{\gamma_z^2} \tag{38}$$

Note that the field measurements are a function of time. Given k field measurements, we can construct k separate equations such as Eq. (38). Rearranging k Eq. (38)-like expressions into a matrix equation of the standard $\mathbf{z}=H\mathbf{x}+\mathbf{v}$ form leads to

$$-\begin{bmatrix} [\hat{h}_x^b(t_1)]^2 \\ [\hat{h}_x^b(t_2)]^2 \\ [\hat{h}_x^b(t_3)]^2 \\ \vdots \\ [\hat{h}_x^b(t_{k-1})]^2 \\ [\hat{h}_x^b(t_k)]^2 \end{bmatrix} = [H_{11}\ H_{12}] \begin{bmatrix} b_x \\ \mu_1 b_y \\ \mu_2 b_z \\ \mu_1 \\ \mu_2 \\ \mu_3 \end{bmatrix} + \mathbf{v} \tag{39}$$

The vector $\mathbf{v}$ represents the measurement noise, and the measurement matrix H consists of two $k\times 3$ submatrices, the first of which, $\mathbf{H}_{11}$, is defined as

$$\mathbf{H}_{11} = \begin{bmatrix} -2\hat{h}_x^b(t_1) & -2\hat{h}_y^b(t_1) & -2\hat{h}_z^b(t_1) \\ -2\hat{h}_x^b(t_2) & -2\hat{h}_y^b(t_2) & -2\hat{h}_z^b(t_2) \\ -2\hat{h}_x^b(t_3) & -2\hat{h}_y^b(t_3) & -2\hat{h}_z^b(t_3) \\ \vdots & \vdots & \vdots \\ -2\hat{h}_x^b(t_{k-1}) & -2\hat{h}_y^b(t_{k-1}) & -2\hat{h}_z^b(t_{k-1}) \\ -2\hat{h}_x^b(t_k) & -2\hat{h}_y^b(t_k) & -2\hat{h}_z^b(t_k) \end{bmatrix} \tag{40}$$

The second submatrix $\mathbf{H}_{12}$ is given by

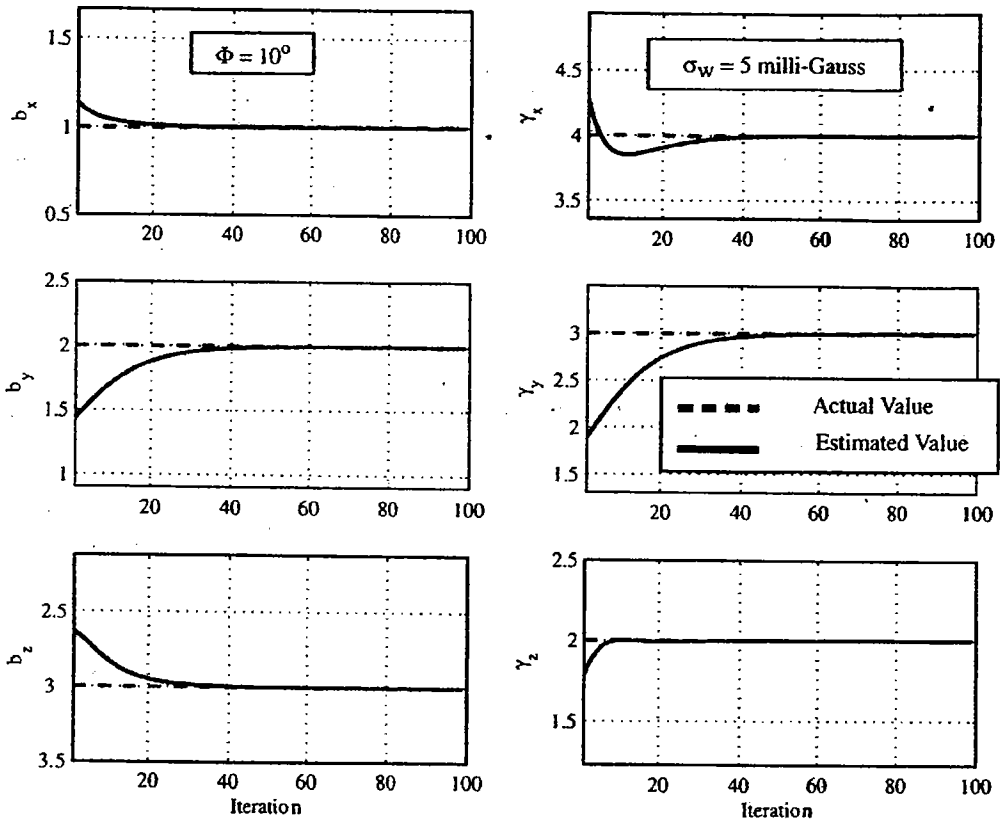

Fig. 7. Hard iron-caused null-shift (in Gauss) and γ (unitless) for iterative least-squares estimator

$$\mathbf{H}_{12}=\begin{bmatrix} [\hat{h}_y^b(t_1)]^2 & [\hat{h}_z^b(t_1)]^2 & 1 \\ [\hat{h}_y^b(t_2)]^2 & [\hat{h}_z^b(t_2)]^2 & 1 \\ [\hat{h}_y^b(t_3)]^2 & [\hat{h}_z^b(t_3)]^2 & 1 \\ \vdots & \vdots & \vdots \\ [\hat{h}_y^b(t_{k-1})]^2 & [\hat{h}_z^b(t_{k-1})]^2 & 1 \\ [\hat{h}_y^b(t_k)]^2 & [\hat{h}_z^b(t_k)]^2 & 1 \end{bmatrix} \tag{41}$$

The vector on the right side of Eq. (39), denoted as $\mathbf{x}$, is the first-step state vector and consists of the variables μ_1 through μ_4, which are defined as follows:

$$\mu_1=\frac{\gamma_x^2}{\gamma_y^2} \tag{42}$$

$$\mu_2=\frac{\gamma_x^2}{\gamma_z^2} \tag{43}$$

$$\mu_3=b_x^2+\mu_1 b_y^2+\mu_2 b_z^2-\mu_4 \tag{44}$$

$$\mu_4=h^2\gamma_x^2=\mu_3-(b_x^2+\mu_1 b_y^2+\mu_2 b_z^2) \tag{45}$$

An estimate for $\mathbf{x}$, denoted as $\hat{\mathbf{x}}$, is obtained by

$$\hat{\mathbf{x}}=(H^T H)^{-1}H^T\mathbf{y} \tag{46}$$

Once the first-step state vector is estimated, $\hat{b}_x$, b_y, $\hat{b}_z$, $\hat{\gamma}_x$, $\hat{\gamma}_y$, and $\hat{\gamma}_z$ are extracted from $\hat{\mathbf{x}}$ by the following inverse relations:

$$\hat{b}_x=\hat{\mathbf{x}}(1) \tag{47}$$

$$\hat{b}_y=\frac{\hat{\mathbf{x}}(2)}{\hat{\mathbf{x}}(4)} \tag{48}$$

$$\hat{b}_z=\frac{\hat{\mathbf{x}}(3)}{\hat{\mathbf{x}}(5)} \tag{49}$$

$$\hat{\gamma}_x=\sqrt{\frac{\mu_4}{h^2}} \tag{50}$$

$$\hat{\gamma}_y=\sqrt{\frac{\mu_4}{\mu_1 h^2}} \tag{51}$$

$$\hat{\gamma}_z=\sqrt{\frac{\mu_4}{\mu_2 h^2}} \tag{52}$$

It was found that Eqs. (39)–(52) provide a very good estimate of the calibration parameters. It is conceivable, therefore, that this initialization algorithm alone can be used as a snapshot solution in lieu of the iterative least-squares solution developed earlier. This was avoided, however, because the two-step formulation as discussed here does not provide an easy way to compute the posterior covariance matrix $\mathbf{P}$, which will be used as a metric for the quality of the calibration. This is because the measurement noise vector $\mathbf{v}$ is the result of squaring the outputs of the magnetometers [i.e., vector on the right side of Eq. (39)] and thus is neither zero mean nor Gaussian distributed. While novel, nonlinear estimation techniques that combine the unscented transformation (Julier 2002) with Kalman (Julier and Uhlmann 1997) or particle filtering (van der Merwe et al. 2000) can be used to di-

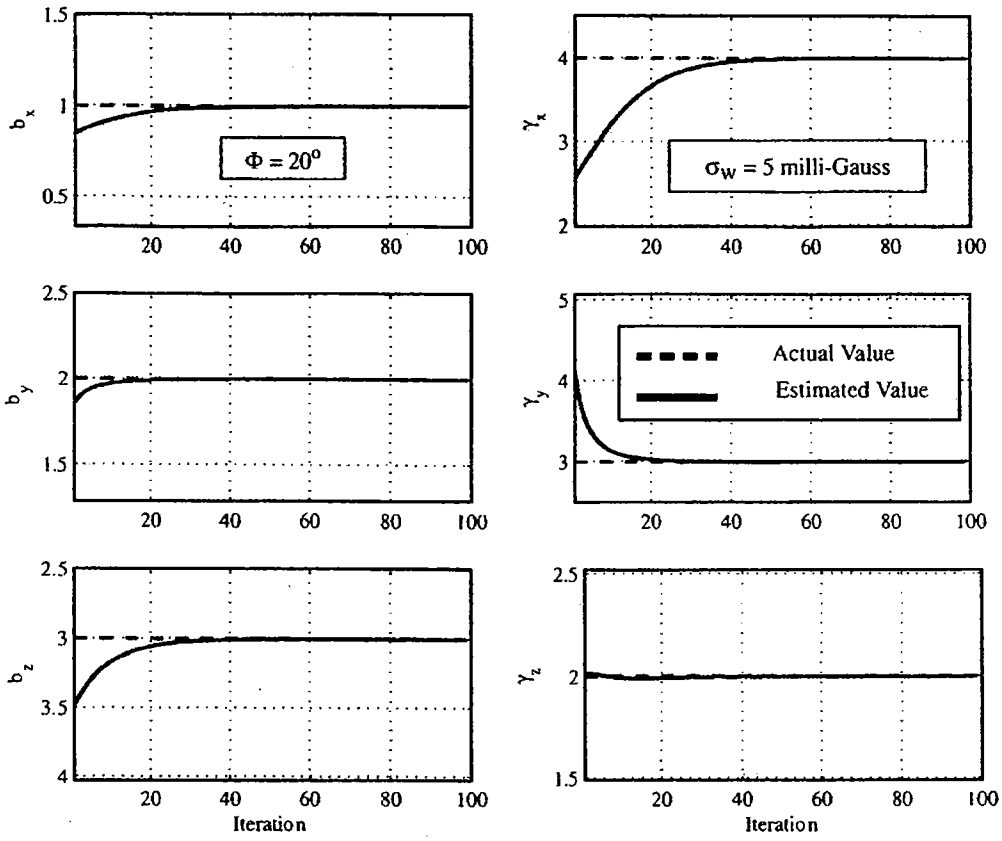

Fig. 8. Hard iron-caused null shift (in Gauss) and γ (unitless) for iterative least-squares estimator

rectly estimate the posterior covariance matrix, for the work reported in this paper, we will use the linearized estimate of **P** given by Eq. (34). As will be shown in the next section, this estimate of **P** generally tends to overbound the actual estimation errors at a $1-\sigma$ level.

Simulation Studies

A series of simulation studies was performed to assess the performance of the magnetometer calibration algorithms. Initially, the performance of the iterative batch least-squares estimator alone was evaluated. The results of this evaluation examine the sensitivity of the iterative batch least-squares estimator to the three factors noted earlier: the quality of the initial values for hard iron bias and γ; sampling and sensor wideband noise; and the shape of the measurement locus.

Recall that the iterative batch least-squares estimator requires an initial guess of hard iron biases (b) and scale-factor/soft iron error terms (γ). This is because the ellipsoid-fitting problem is highly nonlinear and thus sensitive to initial values of hard iron bias and γ. The first set of simulation studies, therefore, evaluated the performance of the algorithm where the initial conditions were chosen randomly without using the two-step nonlinear estimator. The initial guesses for the hard iron biases were picked from a normal distribution with a mean equal to the actual biases and a standard deviation of 0.5 Gauss. Similarly, the initial guesses for the scale-factor/soft iron error term, γ, were picked from a normal distribution centered at the actual value of γ with a standard deviation of 0.5.

Two values of measurement noise standard deviation, σ_w, were evaluated. One of the values considered was 5 milli-Gauss and is based on the data shown in Fig. 3. The data shown in Fig. 3, however, were collected on a system that used a digital prefilter to process field measurements before they were recorded. In the absence of such a filter, the value of the wideband noise can be as high at 10 milli-Gauss. As such, the second value of σ_w considered was 10 milli-Gauss.

Fig. 5 is a schematic that illustrates the metric used for quantifying the measurement locus geometry. If during the calibration procedure the magnetometer assembly is rotated through space such that the entire Euler angle space is spanned, the locus of magnetometer measurements obtained would be as shown in Fig. 5(a). As can be seen from the experimental data shown in Fig. 6, this is not always possible, as Fig. 6 shows only a small portion of the ellipsoid. Thus, for the simulation studies we will also assume that only a small portion of the ellipsoid is present [Fig. 5(b)]. The central angle spanned by the strip of the ellipsoid, Φ, is used to characterize the geometry of the measurement locus [Fig. 5(c)].

Table 1 shows the four cases simulated to quantify estimation accuracy as a function of the three sensitivity factors discussed above. The results of these trade-off studies are shown in Figs. 7–13. Figs. 7 and 8 show the performance of the iterative batch least-squares estimator in the presence of a 5 milli-Gauss wideband noise and when 10° and 20° strips of measurement locus are available. While these figures show cases where the algorithm

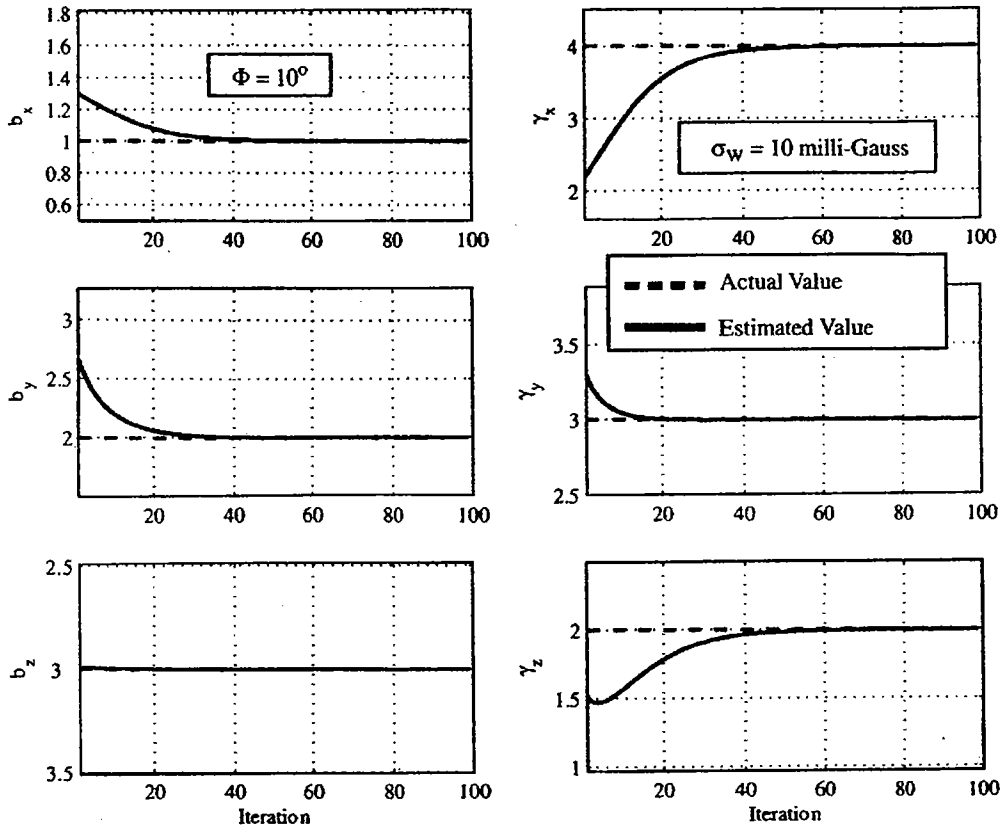

Fig. 9. Hard iron-caused null shift (in Gauss) and γ (unitless) for iterative least-squares estimator

converged, there were instances when the algorithm diverged. The frequency of divergence increases as the wideband noise on the magnetometer measurements increases, as shown in Figs. 9–11. In these figures the noise is increased to 10 milli-Gauss. While the algorithm converged for the particular runs shown in Figs. 9 and 10, it diverged for the run shown in Fig. 11.

The rate of divergence was observed to be higher for $\Phi=10°$ than $\Phi=20°$. For example, in one simulation study, which consisted of 1,000 runs, the divergence rate was approximately 1.5 times greater for the $\Phi=10°$ case when compared to $\Phi=20°$. This is not surprising because at 10 milli-Gauss the estimator will have a harder time distinguishing features of the ellipsoid from noise. This is particularly true when the initial conditions assigned to hard iron biases and γ are too far away from the actual values. This is confirmed when we note that in Figs. 9–11 the initial conditions are not the same because, as noted earlier, the initial conditions were varied randomly from one try to the next. Observe, for example, that the initial conditions assigned to b_x and b_y for the run shown in Fig. 9 are closer to the actual values than assigned for the run shown in Fig. 11.

Precise quantification of the divergence rate of the algorithm due to initial condition errors was not deemed important because, as will be shown later, initializing the algorithm with the two-step estimator eliminates divergence due to initial condition errors. Nevertheless, from Figs. 9–11 we conclude that for relatively low-cost magnetometers with relatively large magnitude output noise, this algorithm is not suitable unless a large portion of the ellipsoid is available. This sensitivity to measurement locus geometry has a very important practical implication. When discussing the methods for calibrating a two-magnetometer system, it was noted that the parameter estimation problem is one where the best circle (in the least-squares sense) is fitted to the noisy magnetometer measurement data. A simple 36° turn on a level surface yielded the required measurement locus.

In extending this method to the 3D case, a tacit assumption was made that the entire sphere would be available for the parameter estimation problem. Unfortunately this is not always the case because getting a complete sphere requires spanning the entire Euler angle space. Thus, unless the magnetometer triad is installed in an aerobatic airplane, spanning the entire Euler angle space is not possible. So the 3D calibration algorithms must be able to work with data that comprise only a portion of the entire sphere. Actual data collected from a flight test are shown in Fig. 6. It is clear from this figure that an entire ellipsoid cannot be obtained in a nonaerobatic aircraft.

The simulation results for the cases where the nonlinear, two-step estimator is used to initialize the iterative batch least-squares estimator are shown in Figs. 12 and 13, which are histograms for the bias and γ estimation errors (or residuals) for 10,000 Monte Carlo simulation runs. For each run, simulated magnetometer outputs were corrupted with bias and scale-factor errors as well as wideband noise. The bias and scale-factor errors were held constant for all 10,000 simulation runs and had the values given in Table 1. The wideband noise, however, was varied for each run in a random sequence with a standard deviation of 5 or 10 milli-Gauss.

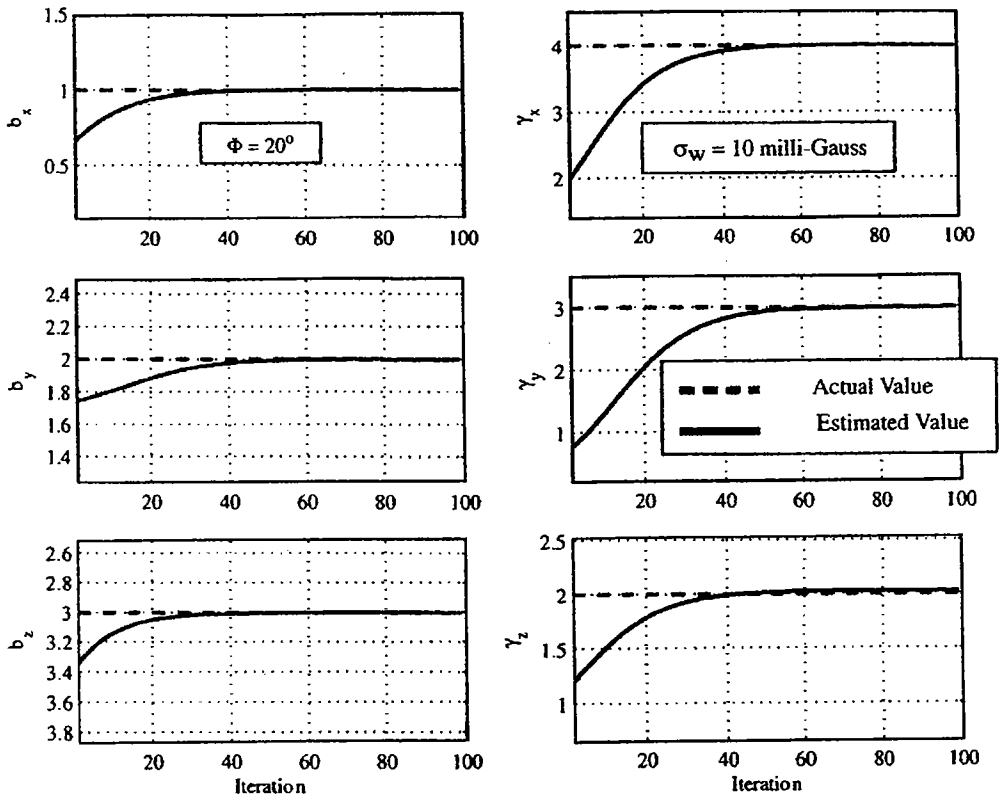

Fig. 10. Hard iron-caused null shift (in Gauss) and γ (unitless) for iterative least-squares estimator

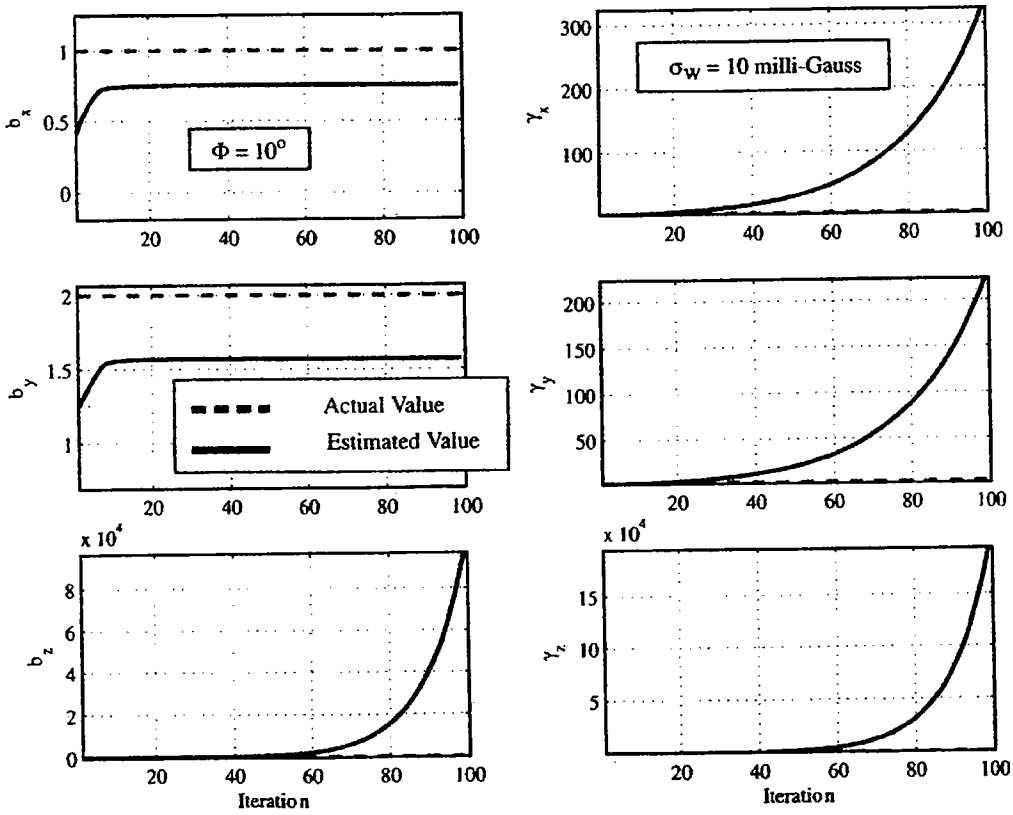

Fig. 11. Divergence of hard iron-caused null shift (in Gauss) and γ (unitless) estimates for iterative least-squares estimator

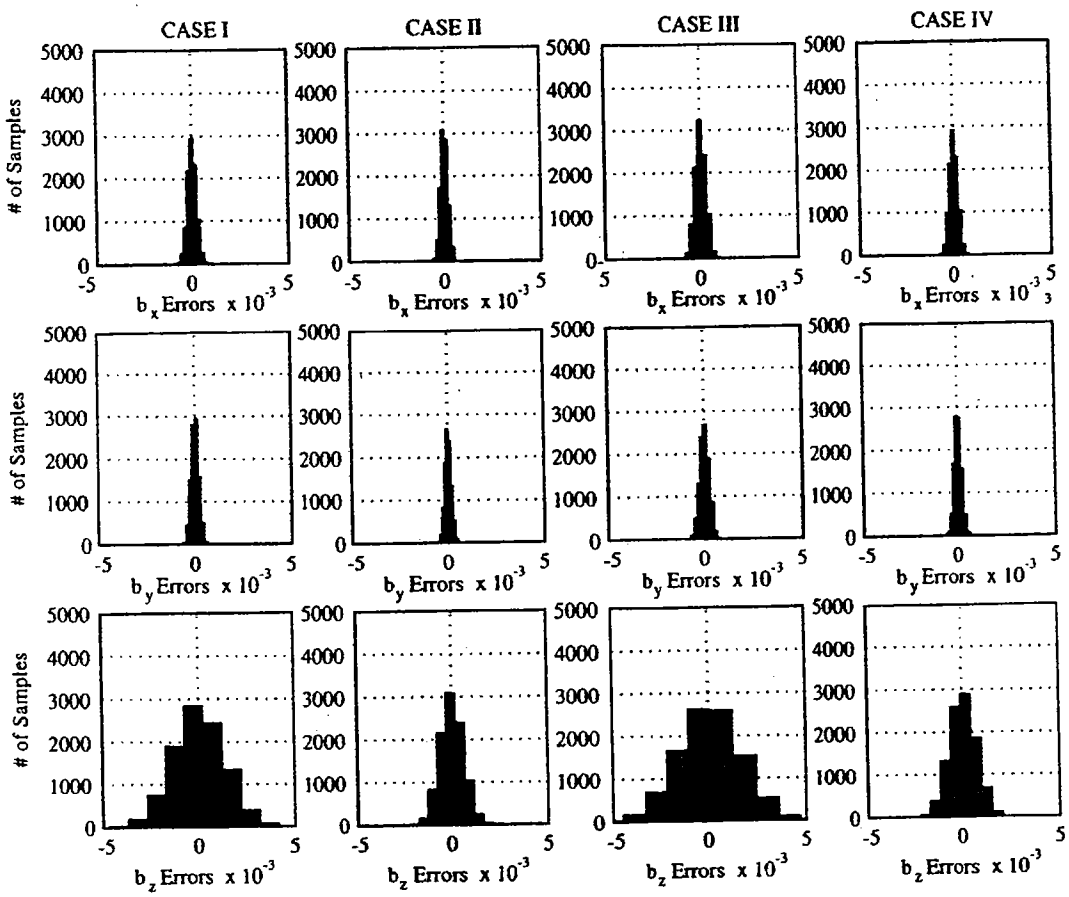

Fig. 12. Hard iron bias estimation errors for when using nonlinear, two-step estimator for initialization (result from 10,000 Monte Carlo runs)

Fig. 12 shows the bias estimation residuals. In none of the 10,000 cases did the solution diverge. For the x and y axes hard iron biases, the estimation errors are seen to be less than ±0.5 milli-Gauss. In comparison to the x and y axes, the z axis estimation errors are slightly larger. However, this error is smaller when the locus of magnetometer measurements is larger. A similar trend is seen in Fig. 13, which shows the scale-factor estimation errors. The fact that the estimation errors for both the z axis hard iron biases and scale-factor errors are larger in comparison to the x and y axis errors is not surprising because even in the 20° locus case the data span only a small amount of space in the z direction.

The $1-\sigma$ standard deviation of the hard iron bias and γ estimation errors for one representative run are summarized in Table 2. The $1-\sigma$ estimation errors are nothing more than the square root of the diagonal elements of the covariance matrix $\mathbf{P}$. As noted earlier and confirmed by observing Figs. 12 and 13 and the data in Table 2, the estimated covariance overbounds the actual errors. Thus, $\mathbf{P}$ can be used as a conservative metric for the quality of the calibration.

In conclusion, initializing the iterative batch least-squares estimator using the nonlinear, two-step estimator is seen to provide superior performance. More specifically, the algorithm does not diverge even in the case when the wideband noise on the magnetometer measurements is large. Thus it requires a smaller portion of the measurement locus than in the case where the iterative least-squares algorithm is used alone.

Experimental Results

As a final verification, a triad of low-cost magnetometers was calibrated using the algorithms developed in this paper. The data were collected from an experimental setup where a set of low-cost magnetometers were strapped to a long wooden boom, as shown in Fig. 14. The wooden boom was used to isolate the magnetometers from magnetic field-generating electronics in the data-collecting computer and associated hardware. To verify the quality of the calibration, the postcalibration heading solution was compared with the heading solution from an expensive navigation grade INS (Honeywell YG1851 IRU). The INS and the experimental set up are shown in Fig. 14.

Fig. 15 shows a histogram of the residuals in the magnetic field domain after the calibration is complete. These residuals were computed by resolving the known magnetic field vector in the area where this calibration took place (i.e., the San Francisco Bay Area) and resolving it into the axes of the magnetometer triad using the precise INS attitude information. The largest residual, which is on the x-axis magnetometer, has a mean of −0.007 Gauss and a standard deviation of 0.004 Gauss.

Fig. 16 shows a 1 min trace comparing the heading solution computed using the magnetometers with the heading solution generated by the INS. The heading residuals for this 1 min trace are less than 3° RMS. Fig. 17 is a histogram of the heading errors for the entire experiment. Note that the heading error has a stan-

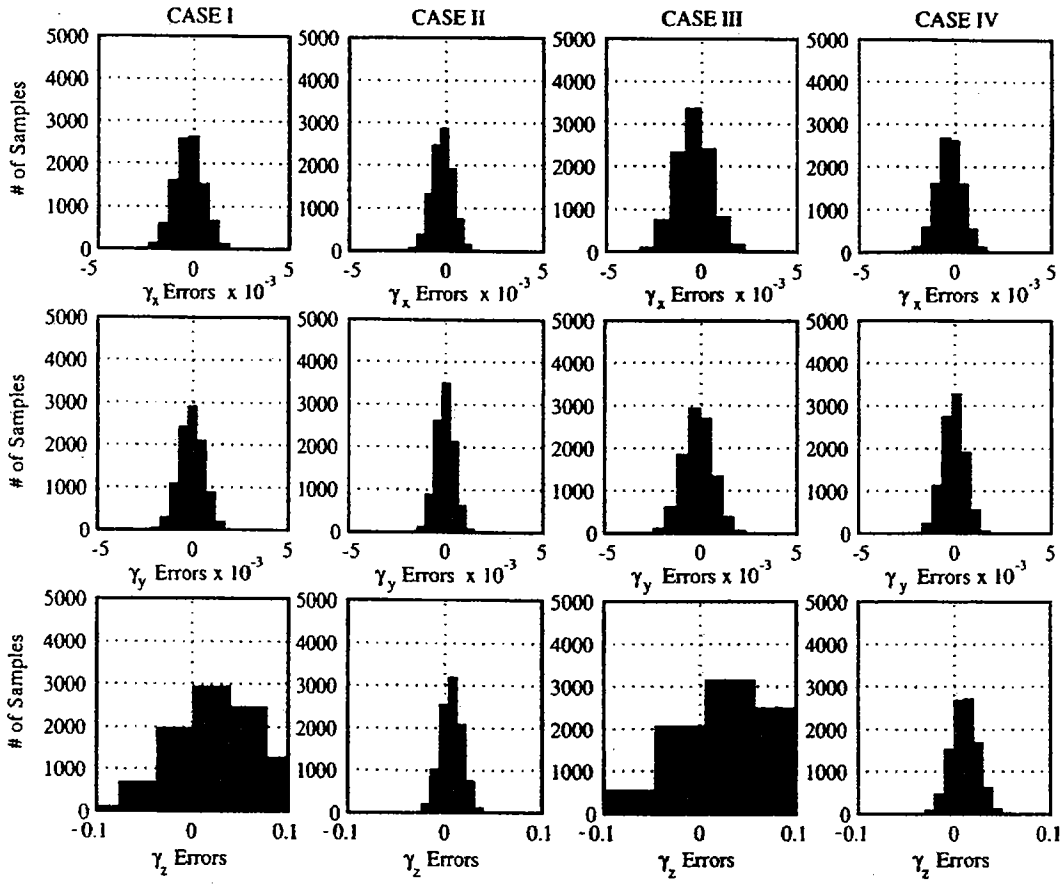

Fig. 13. Scale factor/soft iron (γ) estimation errors when using nonlinear, two-step estimator for initialization (errors are unitless)

dard deviation of 3.6° and a mean of 1.2°. The largest heading error observed was 18° and was the result of the wooden boom flexing relative to the INS (i.e., the truth reference) during the data collection maneuvers. Once the mean is removed, the remaining heading error is, to a large extent, in the form of wide-band noise that can be easily filtered using a a low-pass filter.

Summary and Conclusions

An algorithm for calibrating strapdown magnetometers used in heading determination systems was developed. Unlike the classic method of compass swinging, which computes a series of heading correction parameters, this algorithm estimates magnetometer

Table 2. State Estimation Errors ($1-\sigma$)

Simulation case	Bias estimation error ($\times 10^{-3}$ Gauss)		γ estimation error (no units)	
I	δb_x	1.73	$\delta\gamma_x$	0.00549
	δb_y	1.30	$\delta\gamma_y$	0.00410
	δb_z	9.00	$\delta\gamma_z$	0.361
II	δb_x	1.34	$\delta\gamma_z$	0.00402
	δb_y	1.01	$\delta\gamma_y$	0.00304
	δb_z	3.90	$\delta\gamma_z$	0.0756
III	δb_x	3.46	$\delta\gamma_x$	0.0108
	δb_y	2.60	$\delta\gamma_y$	0.00809
	δb_z	1.70	$\delta\gamma_z$	0.631
IV	δb_x	2.70	$\delta\gamma_x$	0.00805
	δb_y	2.03	$\delta\gamma_y$	0.00606
	δb_z	7.55	$\delta\gamma_z$	0.143

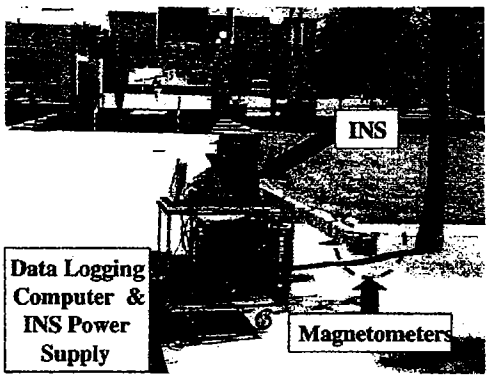

Fig. 14. Experimental setup for ground test

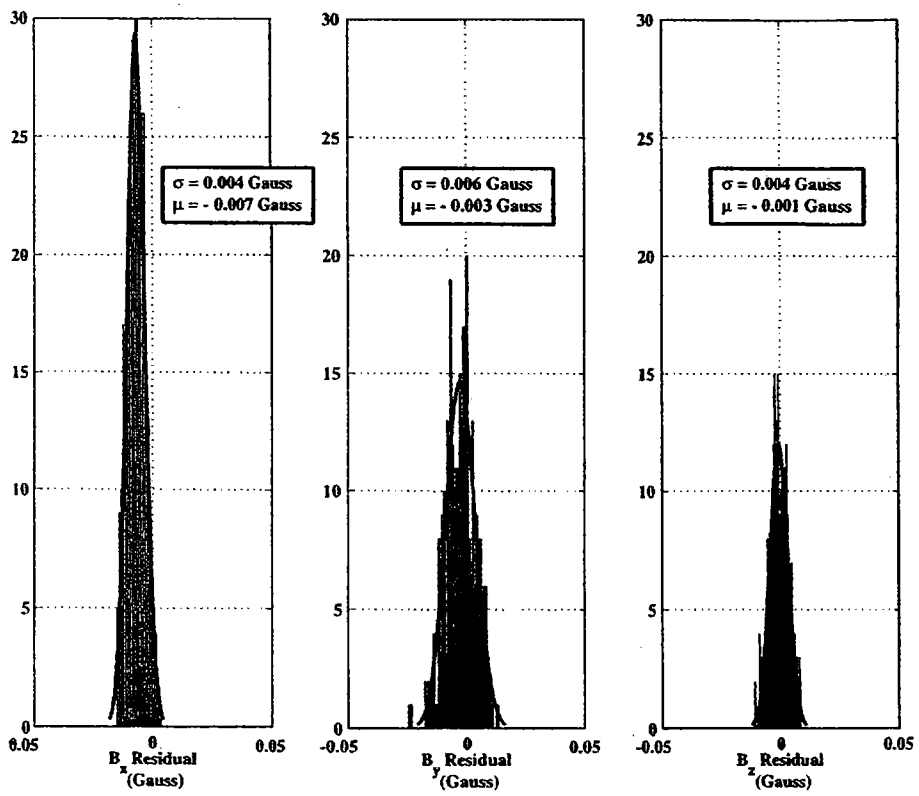

Fig. 15. Magnetometer calibration residuals

output errors directly and thus is not limited to heading determination systems.

The calibration algorithm uses an estimator where the states are the hard iron biases, soft iron biases, and scale-factor errors. The estimator is a linearized, iterative batch least-squares estimator. The initial conditions for the estimator are established using a nonlinear, two-step estimator. When thus initialized, Monte Carlo simulations show the estimation procedure to be very robust.

As presented in this paper, the calibration algorithm is limited to estimation of the hard iron biases and combined scale factor and some soft iron effects. However, it should be possible to extend the applicability of this method to all magnetometer errors, including misalignment and all soft iron errors.

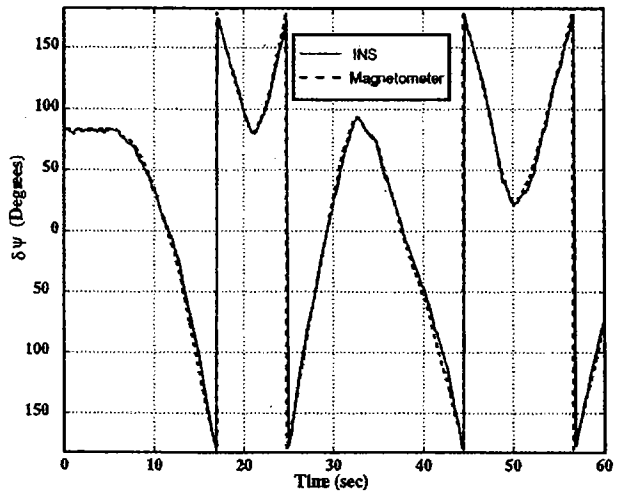

Fig. 16. Comparison of INS and magnetometer headings after calibration

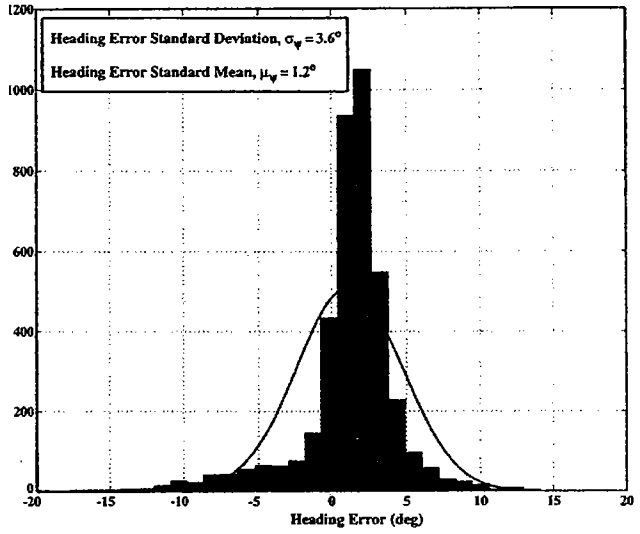

Fig. 17. Histogram of postcalibration heading errors

Acknowledgments

The writers wish to acknowledge the FAA Satellite Navigation Product Team and the Office of Technology and Licensing at Stanford University for sponsoring the research reported in this paper.

Appendix. Compass Swinging Equations

In this appendix, we derive Eqs. (6) and (7), which are used in the compass swinging algorithm. In what follows, it will be assumed that the pair of magnetometers are level and there are no misalignment errors. The effect of misalignment errors will be considered later. A level and error-free pair of magnetometers measures the strength of the horizontal component of the local Earth magnetic field vector, $\mathbf{h}_h$. The measurement made by each of the magnetometers will be

$$h_x^b = h_h \cos(\psi) \tag{53}$$

$$h_y^b = -h_h \sin(\psi) \tag{54}$$

where $h_h = \|h_h\|$ Since the magnetometer assembly is assumed to be level, the body coordinate system is the same as the wander-azimuth coordinate system and h_x^b and h_y^b can be used in lieu of h_x^w and h_y^w in Eq. (1).

If measurement errors are present, the output from the magnetometers in the body frame will not be equal to h_x^b and h_y^b given by Eqs. (53) and (54). Instead, the output of the x-magnetometer will be $\hat{h}_x^b$:

$$\begin{aligned}\hat{h}_x^b &= h_x^b + \delta h_{x_0} + \alpha_{xx} h_x^b + \alpha_{xy} h_y^b \\ &= h_x^b + \delta h_{x_0} + \alpha_{xx} h_H \cos\psi - \alpha_{xy} h_h \sin\psi\end{aligned} \tag{55}$$

Similarly, the y-magnetometer output will be $\hat{h}_y^b$

$$\begin{aligned}\hat{h}_y^b &= h_y^b + \delta h_{y_0} + \alpha_{yx} h_x^b + \alpha_{yy} h_y^b \\ &= h_y^b + \delta h_{y_0} + \alpha_{yx} h_H \cos\psi - \alpha_{yy} B_H \sin\psi\end{aligned} \tag{56}$$

The terms δh_{x_0} and δh_{y_0} represent the hard iron biases while the remaining terms account for errors due to soft iron. Our objective is to evaluate heading errors as a function of magnetometer measurement errors. An expression relating heading errors to magnetometer measurement errors can be arrived at by taking a perturbation of Eq. (1). This leads to

$$\delta\psi = \left(\frac{\partial\psi}{\partial h_y}\right)\delta h_y + \left(\frac{\partial\psi}{\partial h_x}\right)\delta h_x = -\frac{1}{h_h}(\delta h_x \sin\psi + \delta h_y \cos\psi) \tag{57}$$

The perturbation quantities δh_x and δh_y represent magnetometer measurement errors and are given by

$$\delta h_x = \hat{h}_x^b - h_x^b \tag{58}$$

$$\delta h_y = \hat{h}_y^b - h_y^b \tag{59}$$

Substituting these values into Eq. (57) and rearranging leads to the following equation for heading error:

$$\begin{aligned}\delta\psi = \left(\frac{\alpha_{xy} - \alpha_{yy}}{2}\right) - \frac{\delta h_{x_0}}{h_h}\sin(\psi) - \frac{\delta h_{y_0}}{h_h}\cos(\psi) \\ + \left(\frac{\alpha_{xx} - \alpha_{yx}}{2}\right)\sin(2\psi) + \left(\frac{\alpha_{yy} - \alpha_{xy}}{2}\right)\cos(2\psi)\end{aligned} \tag{60}$$

This reduces to Eq. (6) when the following substitutions are made:

$$A = \left(\frac{\alpha_{xy} - \alpha_{yy}}{2}\right) \tag{61}$$

$$B = \frac{\delta h_{x_0}}{h_h} \tag{62}$$

$$C = \frac{\delta h_{y_0}}{h_h} \tag{63}$$

$$D = \left(\frac{\alpha_{xx} - \alpha_{yx}}{2}\right) \tag{64}$$

$$E = \left(\frac{\alpha_{yy} - \alpha_{xy}}{2}\right) \tag{65}$$

Up to this point, misalignments have been ignored. Misalignment errors can be classified into two categories. The first category is the case of pitch-and-roll misalignments, which are installation errors that result in the magnetometers not being level when the vehicle is level. The 2D dimensional swinging algorithm cannot deal with pitch-and-roll misalignments because the errors introduced by such misalignments are time varying. The second category is a yaw misalignment, which is the case where installation errors result in the magnetometer assembly being installed with an azimuth bias. Mathematically, a constant azimuth bias, $\delta\psi_0$, due to installation errors modifies Eq. (60) in the following manner:

$$\begin{aligned}\delta\psi = A + B\sin(\psi + \delta\psi_0) + C\cos(\psi + \delta\psi_0) + D\sin(2\psi + 2\delta\psi_0) \\ + E\cos(2\psi + 2\delta\psi_0)\end{aligned} \tag{66}$$

When this equation is expanded using trigonometric identities and rearranged, one gets

$$\delta\psi = \bar{A} + \bar{B}\sin(\psi) + \bar{C}\cos(\psi) + \bar{D}\sin(2\psi) + \bar{E}\cos(2\psi) \tag{67}$$

which is identical to Eq. (6) except that the coefficients are now modified. Thus, swinging can deal with yaw misalignments. This also implies that a compass rose is not really required when using a swinging algorithm. All that is required is to swing the magnetometer assembly through equally spaced headings around the compass rose followed by one final known heading. In this instance, the offset term, $\delta\psi_0$, will be the sum of the installation error and the constant heading error introduced by the fact that a compass rose was not used. Thus, the final known heading is used to separate the two individual components of $\delta\psi_0$.

References

Barton, C. E. (1997). "International geomagnetic reference field: The seventh generation." *J. Geomagn. Geoelectr.*, 49, 123–148.

Bowditch, N. (1984). *The American practical navigator*, Hydrographic/

Topographic Center, Defense Mapping Agency, Bethesda, Md., 201–259.

Eberly, D. (2001). *Least squares fitting of data*, Magic Software, Inc., Chapel Hill, N.C.

Elkaim, G. H. (2001). "System identification for precision control of a GPS-autonomous catamaran." Ph.D. dissertation, Dept. of Aeronautics and Astronautics, Stanford Univ., Stanford, Calif.

Gebre-Egziabher, D. (2001). "Design and performance analysis of a low-cost aided-dead reckoning navigation system." Ph.D. dissertation, Dept. of Aeronautics and Astronautics, Stanford Univ., Stanford, Calif.

Gebre-Egziabher, D. Elkaim, G. H., Powell, J. D., and Parkinson, B. W. (2001a). "A gyro-free quaternion-based attitude determination system suitable for implementation using low-cost sensors." *Proc., IEEE Position Location and Navigation Symp. (PLANS2000)*, 185–192.

Gebre-Egziabher, D., Elkaim, G. H., Powell, J. D., and Parkinson, B. W. (2001b). "A non-linear, two-step estimation algorithm for calibrating solid-state strapdown magnetometers." *Proc., 8th Int. Conf. on Integrated Navigation Systems*, 200–299.

Haupt, G. T. (1996). "Development and experimental verification of a nonlinear data reduction algorithm for gravity probe B relativity mission." Ph.D. dissertation, Dept. of Aeronautics and Astronautics, Stanford Univ., Stanford, Calif.

Julier, S. J. (2002). "The scaled unscented transformation." *Proc., American Control Conf.*, 4555–4559.

Julier, S. J., and Uhlmann, J. K. (1997). "A new extension of the Kalman filter to nonlinear systems." *Proc., 11th Int. Symp. on Aerospace/Defence Sensing, Simulation and Controls*, 182–193.

Kaplan, W. (1952). *Advanced calculus*, Addison-Wesley, Reading, Mass., 86–88.

Kayton, M., and Fried, W. R. (1997). *Avionics navigation systems*, 2nd Ed., Wiley, New York, 436–444.

LITEF Corp. (2001). *LCR-92 attitude heading reference system*, Freiberg, Germany.

Siouris, G. M. (1993). *Aerospace avionics systems: A modern synthesis*, Academic, San Diego, Calif., 41–48.

van der Merwe, R., Doucet, A., de Freitas, J. F. G., and Wan, E. (2000). "The unscented particle filter." *Technical Rep. CUED/F-INFENG/TR 380*, Engineering Dept., Cambridge Univ., Cambridge, U.K.